Article

Enhanced Electrochemical Properties of Na$_{0.67}$MnO$_2$ Cathode for Na-Ion Batteries Prepared with Novel Tetrabutylammonium Alginate Binder

Gints Kucinskis [1],* , Beate Kruze [1] , Prasad Korde [1,2], Anatolijs Sarakovskis [1], Arturs Viksna [3], Julija Hodakovska [1] and Gunars Bajars [1]

[1]   Institute of Solid State Physics, University of Latvia, LV-1063 Riga, Latvia; beate.kruze@cfi.lu.lv (B.K.); korde@kth.se (P.K.); anatolijs.sarakovskis@cfi.lu.lv (A.S.); julijah@cfi.lu.lv (J.H.); gunars.bajars@cfi.lu.lv (G.B.)

[2]   Department of Chemical Engineering, Division of Applied Electrochemistry, KTH Royal Institute of Technology, SE-10044 Stockholm, Sweden

[3]   Department of Analytical Chemistry, Faculty of Chemistry, University of Latvia, LV-1004 Riga, Latvia; arturs.viksna@lu.lv

*   Correspondence: gints.kucinskis@cfi.lu.lv

Abstract: Both the binder and solid–electrolyte interface play an important role in improving the cycling stability of electrodes for Na-ion batteries. In this study, a novel tetrabutylammonium (TBA) alginate binder is used to prepare a Na$_{0.67}$MnO$_2$ electrode for sodium-ion batteries with improved electrochemical performance. The ageing of the electrodes is characterized. TBA alginate-based electrodes are compared to polyvinylidene fluoride- (PVDF) and Na alginate-based electrodes and show favorable electrochemical performance, with gravimetric capacity values of up to 164 mAh/g, which is 6% higher than measured for the electrode prepared with PVDF binder. TBA alginate-based electrodes also display good rate capability and improved cyclability. The solid–electrolyte interface of TBA alginate-based electrodes is similar to that of PVDF-based electrodes. As the only salt of alginic acid soluble in non-aqueous solvents, TBA alginate emerges as a good alternative to PVDF binder in battery applications where the water-based processing of electrode slurries is not feasible, such as the demonstrated case with Na$_{0.67}$MnO$_2$.

Keywords: sodium-ion batteries; alginate; Na$_{0.67}$MnO$_2$; binder; cathode

1. Introduction

Energy storage systems that are made from abundant materials are essential for the transition to a more sustainable economy. Although lithium-ion batteries (LIBs) are by far the most popular battery technology, the low availability of lithium, as well as use of cobalt and other rare metals raise questions on the sustainability and long-term viability of LIBs as the only energy storage solution. With the high abundance of sodium and relative similarity to LIBs, sodium-ion batteries (SIBs) are emerging as a suitable battery technology for stationary energy storage [1]. The widespread adoption of the SIB technology, however, is hampered by many challenges, including the relatively low energy density or service life compared to LIBs. Lower energy density cathodes, such as Na$_2$FeP$_2$O$_7$ or NaFePO$_4$, are generally stable during cycling [2,3], while the cycle life of many of the higher energy density cathodes (e.g., transition metal oxides Na$_x$MO$_2$ where M—transition metal) has so far been subpar [4], so advances in material and electrode engineering are still required.

In most battery electrodes, a binder is used to assure a mechanically stable contact between the current collector, active material, and electron-conducting additives. The good electrochemical stability in the 0–5 V range, chemical resistance in electrolyte, durable adhesion to current collector, and good binding between PVDF and active electrode materials

make polyvinylidene fluoride (PVDF) one of the most popular binder choices for LIBs, so PVDF is also often used in SIBs. However, PVDF-based electrodes cannot tolerate the large volume changes that some of the current electrode materials undergo upon charging and discharging [5]. Moreover, in SIBs, PVDF is shown to undergo defluorination if no additional source of fluorine is available [6], so alternative binders are starting to emerge. Organic compounds, such as carboxymethyl cellulose (CMC), styrene butadiene rubber (SBR) and alginate compounds have been reported [7]. Due to their improved mechanical properties and chemical stability, these new binders often offer better cycle life, higher capacity, and rate capability.

Among alginate compounds, sodium alginate [8], the sodium salt of alginic acid, a compound that is obtained from the cell walls of brown algae, is by far the most studied. It can extend the cycle life of many battery materials due to its higher mechanical strength (as shown in studies on Si anode for LIBs [9,10]), as well as by forming a more uniform protective coating on the particles of the active material [11–13]. An added benefit is Na alginate's solubility in water, enabling preparation of aqueous electrode slurries and thus ensuring environmentally friendlier preparation of electrodes. Unfortunately, organic solvents are not able to dissolve Na alginate. This makes the Na alginate binder incompatible with many of the SIB electrodes that decompose rapidly if exposed to air or water, promoting the search for a compound that would combine the favourable properties of Na alginate while also enabling the preparation of anhydrous electrode slurries.

The instability in water is perhaps best exemplified by layered metal oxide cathodes, such as P2-type $Na_{0.67}MnO_2$ [14]. Capacity-wise, P2-type $Na_{0.67}MnO_2$ is a very competitive SIB cathode, with high practical gravimetric capacity in the range of 160–200 mAh/g [15]. At the average discharge potential of 2.75 V vs. Na/Na^+, this results in material energy density of up to 550 Wh/kg. Actual measured capacities are a subject to the chosen voltage range, which is in turn often a compromise between specific charge capacity and cycle life. First investigated in 1999 by Paulsen et al. [16], it has received increased attention from the scientific community over the last five years. Luo et al. showed a capacity of roughly 160 mAh/g and cycle life decrease of roughly 50% over 500 full charge-discharge cycles over a narrow 2.0–3.8 V vs. Na/Na^+ range as well as improvement when substituting some Mn with Fe and Ni [17]. Lyu et al. demonstrated that the cycle life of $Na_{0.67}MnO_2$ can be significantly improved when switching to solid electrolyte [18]. More recently, materials engineered on nanoscale, such as nanoplatelets [19] and other nanostructures [20,21], have displayed increased rate capability, albeit with only marginal improvements in cycle life and overall capacity. On average, $Na_{0.67}MnO_2$ lost around 15% of its capacity over first 100 charge-discharge cycles. Doping has yielded improvements regarding cycle life and stability in air. For example, doping with Co [22], Ni, and Mg [23] has been somewhat effective. Creating higher charge-discharge potentials by substituting Mn with Ni, Cu, or Fe [24] have yielded promising results. A more detailed review on recent progress in development of cathodes for SIBs can be found in references [25,26].

The underlying reason why Mn in $Na_{0.67}MnO_2$ is often partly replaced by Ni, Fe, Ti, Al, Mg, and other metals [21,23,27–30] is the attempt to improve its cycle life. The cycle life of pristine P2-type $Na_{0.67}MnO_2$ is known to be relatively bad due to the gliding and reordering of crystalographic planes at the highly charged states, that lead to P2-P2′, P2-O2, or P2-OP4 phase transitions [21,29]. Doping and Mn substitution lead to altered interlayer spacing and thus altered O-O repulsion and O-Na attraction forces that lead to changes in the structural stability of $Na_{0.67}MnO_2$ [31].

The same effect of changing interlayer spacing take place upon exposing $Na_{0.67}MnO_2$ to water. However, the structural changes happen to such an extreme degree that the P2-type $Na_{0.67}MnO_2$ structure eventually disintegrates. Upon exposure to water, Na^+ in $Na_{0.67}MnO_2$ is displaced by H^+, changing the interlayer spacing, causing crystallographic planes to glide and leading to the phase transformation of $Na_{0.67}MnO_2$ [24,32]. Ultimately, proton intercalation increases interlayer distance to the point where water molecules can be inserted in the interlayer space [24,33], leading to decomposition of the original P2-type

crystal structure, and the cathode loses its capacity for reversible extraction and insertion of Na. There have been signs of a certain water exposure having a positive effect on the stability and rate capability of $Na_{0.67}MnO_2$ due to increased interlayer spacing [31]. However, without any modifications, treating pristine $Na_{0.67}MnO_2$ in water or even just storing it in air leads to the significant worsening of electrochemical properties. Similar effects are observed in polyanionic Na-ion cathodes.

Although aqueous electrode preparation shows promise in some areas, the described challenges promote a search for alternative binders that are stable in contact with the active materials, do not decompose in the voltage range of 2.0–4.3 V, and are soluble in non-aqueous solvents to assure the stability of the active material. Here, for the first time, we demonstrate tetrabutylammonium (TBA) alginate, a TBA salt of alginic acid [34], as a suitable alternative to PVDF and Na alginate. TBA alginate is soluble in water as well as dimethyl sulfoxide (DMSO) [34], N,N-dimethylformamide [35], and other polar aprotic solvents containing tetrabutylammonium fluoride [36], making it the only currently reported alginate that is soluble in non-aqueous solvents. As shown in this work, TBA alginate can open new opportunities for the non-aqueous processing of SIB cathode slurries and demonstrates promising capacity and cyclability improvements over the PVDF-based electrodes.

2. Results

2.1. Morphology and Structure of $Na_{0.67}MnO_2$

The Na-Mn molar ratio in the as-obtained material corresponds to $Na_{0.66\pm0.02}MnO_2$ according to ICP-MS results. The synthesized powder is black and has the P2-type layered structure of $Na_{0.67}MnO_2$, as verified by x-ray diffraction (XRD) and shown in Figure 1a. Rietveld analysis of the XRD pattern confirms the correspondence to the hexagonal crystal lattice with P63/mmc space group (space group no. 193) as first observed by Paulsen et al. [16]. The refined lattice parameters are a = 2.87217 Å and c = 11.11251 Å with no impurity peaks detected. R_{wp} = 4.6% and R_B = 2.4% factors are reasonably small.

(a)　　　　　　　　　　　　　　　　　　　　　　　　　　(b)

Figure 1. *Cont.*

(**c**)

(**d**)

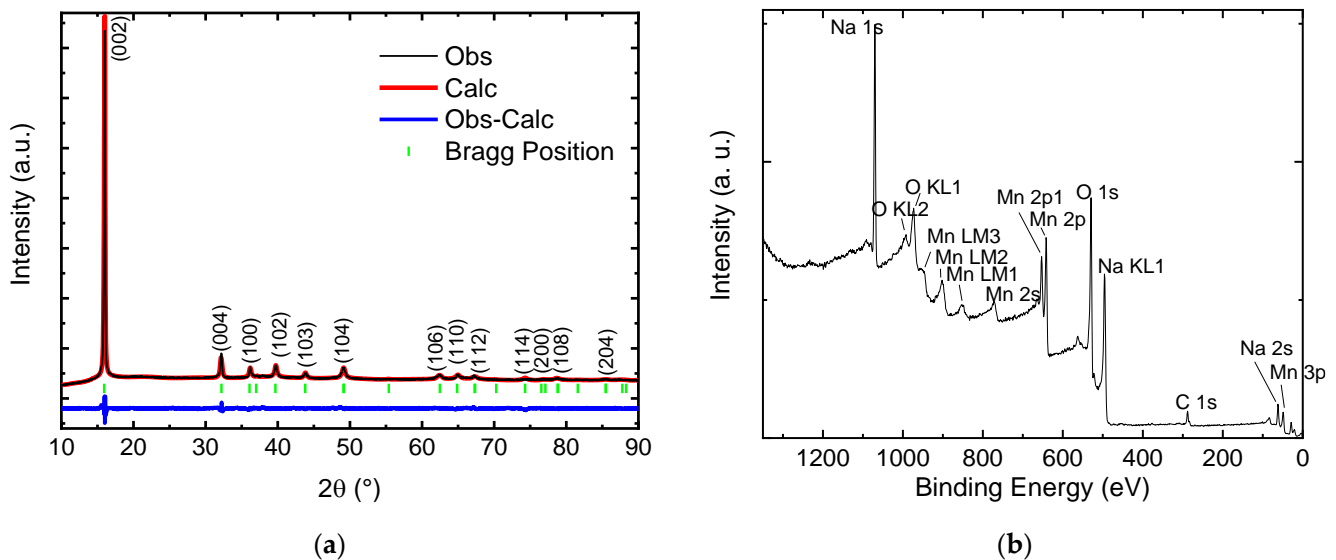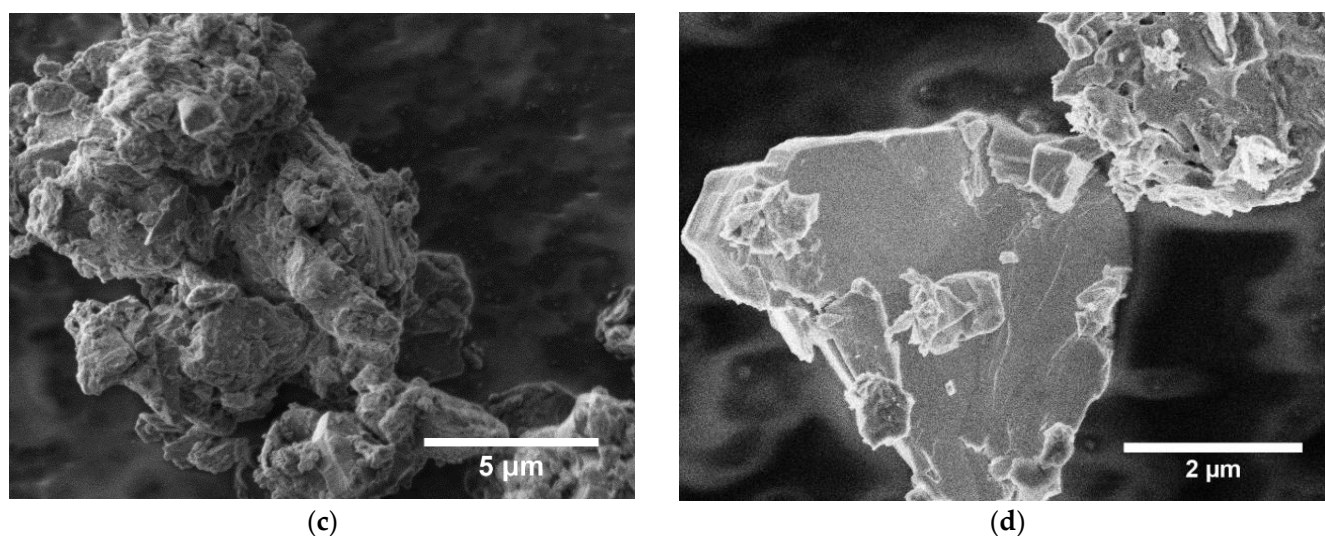**Figure 1.** Structural, compositional and morphological data of the synthesized $Na_{0.67}MnO_2$ cathode: (**a**) XRD data and Rietveld refinement—all peaks can be indexed with the layered P2-type structure of $Na_{0.67}MnO_2$ as reported by Paulsen et al. [16]; (**b**) XPS survey shows presence of all elements present in $Na_{0.67}MnO_2$; (**c,d**) SEM images indicate a grain size of 1–5 μm.

XPS results of the as-prepared $Na_{0.67}MnO_2$ confirm the presence of Na, Mn and O along with trace amounts of carbon (Figure 1b). Individual peaks of Na, Mn, O, and C are shown in Supplementary Information, Figure S1. Mn 2p signal is analysed, and the deconvoluted peaks are consistent with Mn signal in $Na_{0.67}MnO_2$ [23]. The energy separation between the Mn $2p_{3/2}$ and Mn $2p_{1/2}$ states is 11.3 eV, similar to that observed in $LiMn_2O_4$ spinels [37]. To determine the oxidation state of manganese species, one can use Mn 3s peaks [38–41]. It has been shown that the separation between the peaks in MnO is in the range of 5.7–5.8 eV, in Mn_2O_3—5.4–5.5 eV, while in MnO_2 the separation can be observed in the range of 4.5–4.9 eV. The experimental values measured here are 83.7 eV and 88.8 eV, corresponding to E = 5.1 eV. The obtained results suggest that the valence state of the manganese species in the material corresponds to a combination of Mn^{3+} and Mn^{4+} (Supplementary Information, Figure S1e). Detailed XPS spectra along with additional discussion are provided in Supplementary Information, Section S1.

Figure 1c,d show the morphology of the as-synthesized powder. Grain size ranges from 1 to 5 μm, and crystallites often have sharp edges. The presence of $NaHCO_3$, NaOH, Na_2CO_3, or any other impurity could not be detected by XRD.

2.2. Synthesis and Characterization of TBA Alginate

The obtained TBA alginate is a slightly yellowish powder, which can be dissolved in DMF (concentration 2 wt.%), ultimately obtaining a solution with no residue present. FTIR data (Figure 2) are in good agreement with the results of Schleeh et al. [42]. After Na alginate is converted to alginic acid, a peak at 1610 cm^{-1} characteristic to carboxylate C-O stretching in Na alginate disappears, while the peak at 1740 cm^{-1} corresponding to saturated COOH becomes visible. As expected, with the synthesis of TBA alginate, the peak of COO^- at 1610 cm^{-1} reappears. While we do not determine the degree of substitution of TBA (DS_{TBA}) in the scope of this paper, we note that a similar synthesis leads to DS_{TBA} values in the range of 0.80–0.95 [42].
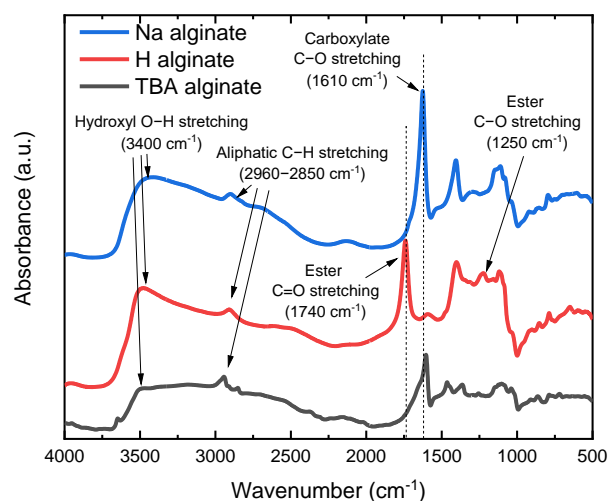
Figure 2. FTIR spectra of powders of alginic acid (H alginate), Na alginate and TBA alginate.

2.3. Preparation of Electrodes

$Na_{0.67}MnO_2$ electrodes were prepared by using TBA alginate and two other binders for reference, PVDF and Na alginate. A homogenous slurry can be obtained within the first 30 min of mixing when using PVDF binder. The mixing is nevertheless continued for 4 h to match the mixing times of electrodes based on alginate chemistries, since slurries with alginate binders were found to require mixing for longer, in order to obtain homogenous electrodes. Although none are used in this study, employing surfactants might be advised in the future work in order to speed up the electrode preparation. As water is quicker to evaporate than NMP or DMF, Na alginate-based electrodes were dried in room conditions initially to avoid electrode cracking. In our experiments, appearance of cracks correlated with significantly worse long term cycling results, so extended drying times (and somewhat longer water exposure) are preferred over a cracked electrode.

Regarding the coating conditions, we found no difference in electrochemical properties (rate capability and long-term cycling) between electrodes coated and handled in Ar-filled glovebox and ambient conditions, likely due to the very limited air-exposure time. See details in Supplementary Information, figures and discussion in Chapter S2.

SEM images of obtained electrodes (Figure 3) indicate that the electrodes are homogeneous, and particles of active material are evenly dispersed within the matrix of the binder and carbon black electron-conducting additive.
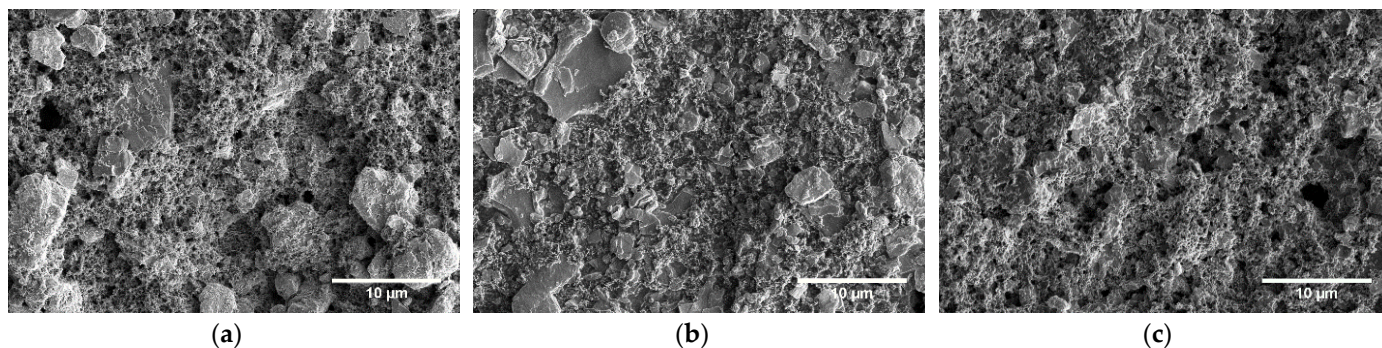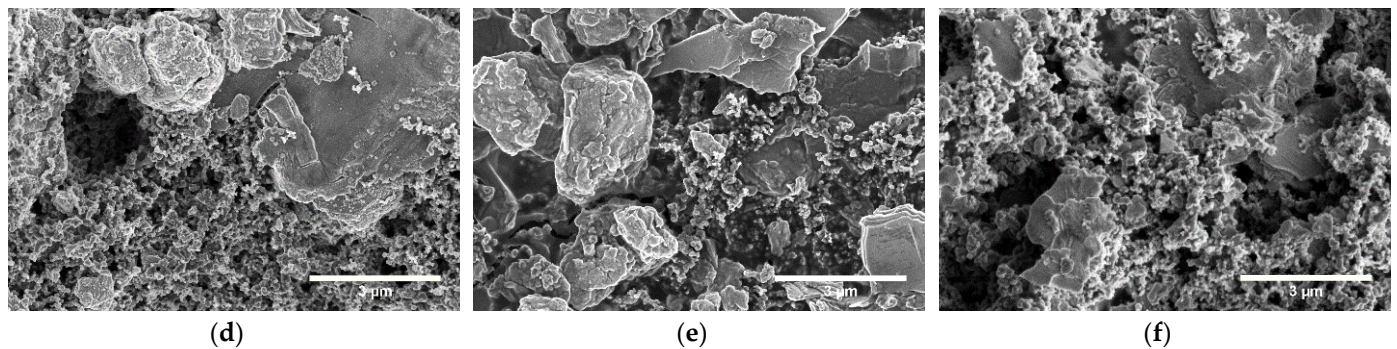

(a)　　　　　　　　　　　(b)　　　　　　　　　　　(c)

Figure 3. *Cont.*

Figure 3. SEM of $Na_{0.67}MnO_2$ electrodes prepared with (**a**,**d**) PVDF; (**b**,**e**) Na alginate and (**c**,**f**) TBA alginate binders. The length of the scale bar is 10 μm for images in the top row and 3 μm for images in the bottom row.

2.4. Electrochemical Properties and Cycling Behaviour

2.4.1. Electrochemical Properties in Standard SIB Half-Cells

First, a baseline is established by assessing the electrodes prepared with PVDF and Na alginate binders. While PVDF-based $Na_{0.67}MnO_2$ displays charge capacity of roughly 155 mAh/g, as shown in Figure 4a, the capacity decreases to 120 mAh/g if Na alginate binder is used (Figure 4b). This is a result of the aqueous preparation route, as $Na_{0.67}MnO_2$ is known to be unstable in water and humidity [24]. We find that the water-unstable $Na_{0.67}MnO_2$ has been partially decomposed by exchanging Na^+ with H^+ and ultimately intercalating H_2O between the Mn-O layers, as confirmed by XRD in Figure 5. While one can speculate that some of the intercalated hydrogen can later be displaced with Na again, it has been shown that air-exposed electrodes display decreased rate capability, gravimetric capacity, and worse cyclability. This is indeed what we see in this study (Figure 4), as the gravimetric capacity of Na alginate-based electrodes is significantly reduced.

The phase associated with water-exposure of Na_xMO_2 (M – transition metal) is birnessite, and it has an increased interlayer distance compared to P2-type $Na_{0.67}MnO_2$ [43]. Further intercalation of water is associated with formation of the buserite phase. Despite the hydrated (birnessite) phase being electrochemically active and capable of storing sodium with a gravimetric charge of at least 84 mAh/g [44], the value is significantly lower than the roughly 160 mAh/g observed for pristine P2-type $Na_{0.67}MnO_2$. As shown in Figure 5, we found that within 4 h of water exposure (4 h is the time needed to ensure proper mixing of electrode slurry), birnessite impurities have already become apparent. If water exposure is continued, after 24 h almost none of the original structure is retained, and most peaks can be attributed to birnessite or buserite phases. A third phase also appears. Although the lack of additional peaks means that we are not able to pinpoint the impurity phase with a reasonable accuracy, the peak is not associated with Na_2CO_3 or $NaHCO_3$. The connection to NaOH or its hydrates, however, cannot be ruled out.

When using TBA alginate binder, we are able to eliminate the exposure to water while still using a salt of alginic acid as a binder. Results in Figure 4c show that electrodes prepared with TBA alginate binder display 6% higher gravimetric capacity, up to 164 mAh/g, with good rate capability when compared to PVDF and Na alginate binders (Figure 4e). In general, the results indicate a good application potential of TBA alginate as a binder for Na-ion batteries. Judged from the charge-discharge curves at 0.1 C (Figure 4d), the overvoltage and thus internal resistances of PVDF and TBA alginate-based $Na_{0.67}MnO_2$ electrodes are similar, while binders with Na alginate display noticeably higher overvoltage and less sharp voltage plateaus, likely a consequence of the partially transformed crystal structure. We are able to observe all voltage plateaus characteristic to $Na_{0.67}MnO_2$ for both TBA alginate and PVDF-based electrodes (Figure 4d).
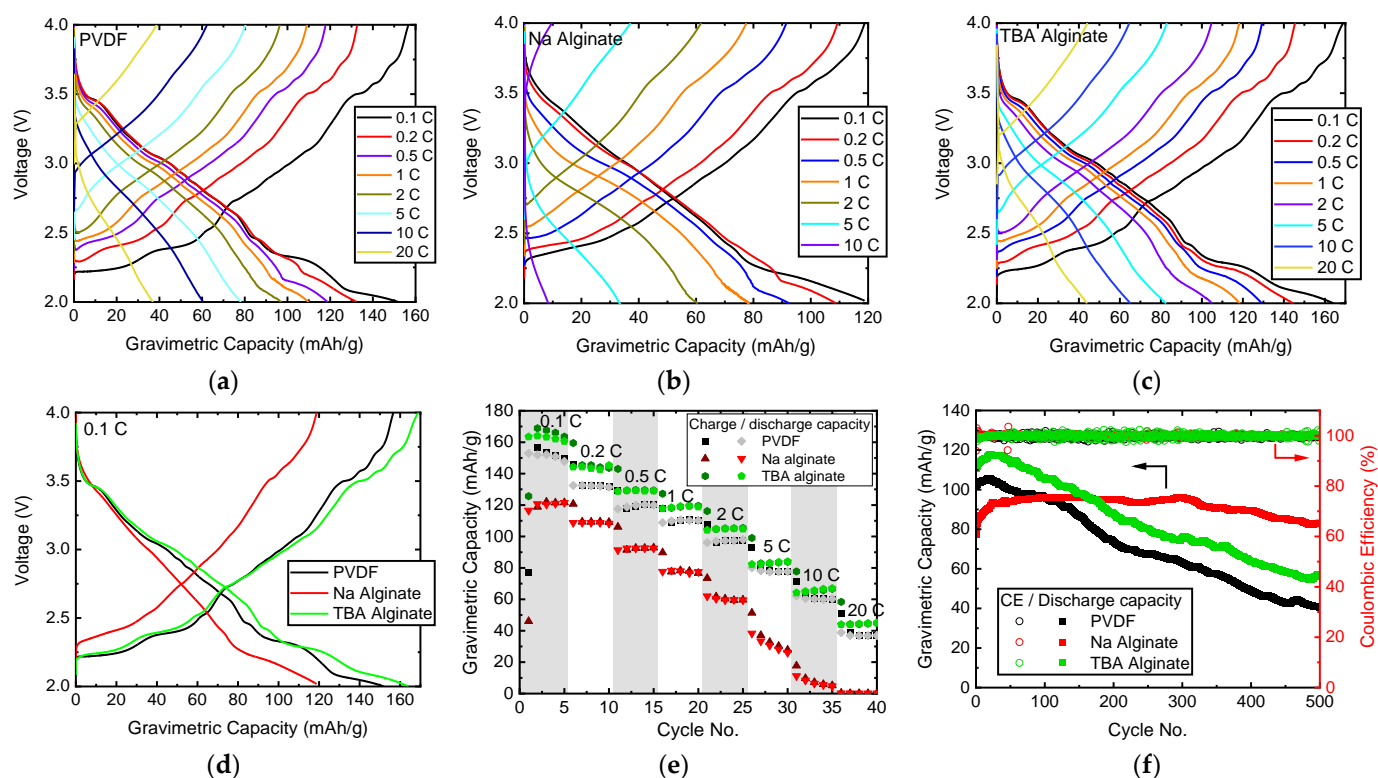
Figure 4. Electrochemical properties of $Na_{0.67}MnO_2$ electrodes prepared with PVDF, Na alginate and TBA alginate binders: charge-discharge curves of $Na_{0.67}MnO_2$ electrodes with (**a**) PVDF binder, (**b**) Na alginate binder, (**c**) TBA alginate binder; (**d**) charge-discharge curves at 0.1 C (17.5 mA/g); (**e**) rate capability of $Na_{0.67}MnO_2$ electrodes; (**f**) cycle life of $Na_{0.67}MnO_2$ electrodes cycled at 1 C; 1 C corresponds to 175 mA/g.

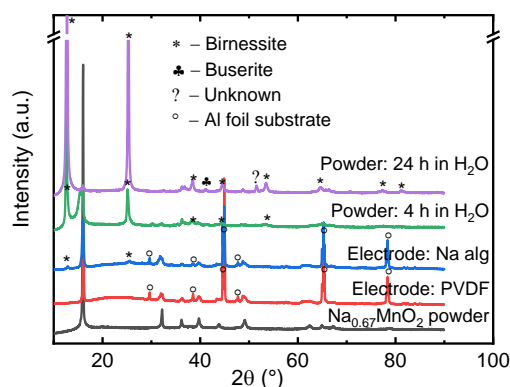**Figure 5.** XRD of $Na_{0.67}MnO_2$ electrodes prepared with PVDF and Na alginate binders, and $Na_{0.67}MnO_2$ powder—pristine and after 4 h and 24 h of water exposure.

The measured specific discharge capacity of TBA alginate-based $Na_{0.67}MnO_2$ electrode is 164 mAh/g at 17.6 mA/g current. This exceeds most of the reported capacities measured within similar voltage window, even doped P2-type $Na_{0.67}MO_2$ materials (M—transition metal oxide) [11,17,21,23,45,46]. Our literature survey also suggests that on average, P2-type $Na_{0.67}MO_2$ compounds see their discharge capacity decrease by 15% over the first 100 cycles. Depending on how this is calculated, we see the discharge capacity decrease by 8–10%, which is at least a 5% reduction in ageing rate. Of course when compared to state-of-art in LIBs, there is still much room for improvement with regard to cycle life. However, we expect that combining TBA alginate binder with $Na_{0.67}MO_2$ [22,31] or

other types of materials for SIBs with higher stability due to doping or other structural modifications can further increase the cycling stability and gravimetric capacity.

The cycling performance of all electrodes, shown in Figure 4f, indicate similarities between electrodes prepared with PVDF and TBA-alginate binders, although the measured absolute gravimetric charge capacity values are higher for TBA alginate-based electrodes. The capacity decreased to 80% of the initial value at cycle 162 for the PVDF-based electrode and cycle 197 for the TBA alginate-based electrode. There is also an initial increase of capacity for both PVDF and TBA alginate-based electrodes, which is higher for TBA alginate. This type of behaviour during first cycles is not uncommon [17,47,48], and is likely related to the formation of a stable SEI on the surface of the electrode, as it has previously been shown to be electrolyte-dependent [48].

As shown in Supplementary Figure S3, the evolution of charge-discharge curves follows a similar pattern for both PVDF and TBA alginate-based electrodes, where the plateaus and other features clearly visible in the initial cycles become less distinct over the cycling and transform somewhat already within the first 20 cycles. This is likely due to irreversible structural changes, induced by discharging in the range of 2.2–2.0 V [15]. The charge-discharge curves of Na alginate-based electrodes are slightly more washed-out.

Somewhat surprisingly, we see the cycling behaviour of Na alginate-based electrode to be significantly improved over PVDF and TBA alginate-based electrodes. The capacity rises form initial 81 mAh/g to 96 mAh/g at 1 C. After 160 cycles the capacity of Na alginate-based electrode surpasses that of TBA alginate-based electrode. After 500 cycles, the capacity of Na alginate-based electrode is still maintained at 82.8 mAh/g or 102% of the initial value. It has been shown that Na alginate can effectively coat the particles of active material, thus preventing several processes: cracking of electrodes, increase in charge-transfer resistance (due to a more stable SEI) and the detachment of electrode from the current collector [11]. It is likely that these are also the reasons behind the improved cycle life of Na alginate-based electrodes in our study. What is somewhat surprising is that this behaviour is not mirrored in TBA alginate-based electrodes, indicating functional differences between TBA alginate and Na alginate.

In order to rule out the improved cyclability of Na alginate-based electrodes coming from the water exposure, we prepared a PVDF-based electrode where $Na_{0.67}MnO_2$ had first been exposed to water in a similar way as while preparing the water-based slurry with Na alginate binder. The electrochemical measurements do not indicate improved cycling performance (see Chapter S4 and Figure S4 in Supplementary Information). Hence, it can be concluded that improvements in long term cycling observed for Na alginate-based electrodes are indeed a consequence of the binder and not the water-exposure of the active material.

The initial Coulombic efficiency is an important parameter for evaluating the performance of electrodes. Measured Coulombic efficiencies are summarised in Table 1. The large values of the initial Coulombic efficiency are not surprising, as $Na_{0.67}MnO_2$ is initially sodium deficient. Assuming that 0.67 parts of Na can be extracted from the electrode, while one full part of Na is inserted in the discharge part of the cycle, the initial Coulombic efficiency should indeed be 149%, in good agreement with the values measured for PVDF and TBA alginate-based electrodes. The initial Coulombic efficiency of Na alginate is somewhat higher, which is consistent with the expected Na loss during aqueous processing of $Na_{0.67}MnO_2$ [24]. Estimated from the observed Coulombic efficiency, the initial stoichiometry of active material in alginate-based electrode is around $Na_{0.4}MnO_2$.

For both alginate-based electrodes, the stabilised Coulombic efficiency is very close to 100. Coulombic efficiency of PVDF-based electrodes also stabilises above 99%, although the determined values are slightly lower than those for alginate electrodes.

Table 1. Coulombic efficiency as a function of cycle and binder material.

Cycle No./C-Rate	Binder Material		
	PVDF	Na Alginate	TBA Alginate
Cycle 1 @ 0.1 C	147.7%	248.9%	157.2%
Cycle 2 @ 0.1 C	98.3%	101.5%	98.5%
Cycle 3 @ 0.1 C	99.4%	99.0%	99.6%
Cycle 4 @ 0.1 C	99.4%	99.9%	99.2%
Cycle 5 @ 0.1 C	98.4%	99.8%	99.9%
Average in cycles 50–100 @ 1 C	$99.8 \pm 0.8\%$	$100.0 \pm 0.2\%$	$99.9 \pm 0.6\%$

2.4.2. TBA Alginate Binder in Other Cell Chemistries

In order to understand the extent to which the improvement of electrochemical properties with TBA alginate binder can be beneficial to other cell chemistries, PVDF, Na alginate, and TBA alginate electrodes were measured in two other cells—SIB half-cell without SEI-stabilising additive added to the electrolyte and LIB half-cell with $LiFePO_4$ cathode.

As the electrolyte chemistries used in Na-ion batteries are more diverse than in LIBs, it is important to note that the measurements reported so far have been performed in $NaClO_4$ electrolyte (1 M $NaClO_4$ salt in propylene carbonate (PC)) containing 5 wt.% fluoroethylene carbonate (FEC) additive. FEC is known to stabilise the electrode–electrolyte interface and prevent the dissolution of PVDF, functioning as an additional source of fluorine that forms NaF interfacial layer [49]. Na alginate can extend the cycle life of electrodes due to uniformly coating the electrode surfaces [11] and preventing parasitic reactions between the electrolyte and electrode. Na alginate is in general not as vulnerable to decomposition as PVDF [50]. To clarify where TBA alginate binder lies in this spectrum, long-term cycling tests were performed in electrochemical cells with 1 M $NaClO_4$ electrolyte in PC without FEC additive. In such conditions, all electrodes display significantly worse cycle life than measured with the FEC-containing electrolyte (Supplementary Information, Chapter S5, Figure S5). The capacities of PVDF, TBA alginate, and Na alginate-based electrodes decrease below 80% of the initial value after 27, 16, and 288 cycles respectively. Since NaF is known to be a crucial part of the SEI [49] and TBA alginate does not contain fluorine, the results are perhaps not too surprising. The obtained data again outline the importance of a stable SEI layer and indicate that the TBA alginate does not provide as strong of an effect on stabilising the SEI layer as Na alginate, where a protective particle coating effect has been suggested [51]. As at no point does the capacity of TBA alginate-based electrode exceed that of PVDF-based, it is likely that the rapid decomposition of the electrode leaves a notable mark already during the first full charge-discharge cycle.

Both initial Coulombic efficiencies (CEs) as well as stabilised CEs are significantly lower than those measured in 1 M $NaClO_4$ electrolyte with 5 wt.% FEC additive (Supplementary Information, Table S1 in Chapter S5). TBA alginate sees the lowest CE, pointing to the most intense parasitic reactions. Na alginate, on the other hand, has the highest CE, consistent with the relatively good long-term cycling results. The results put TBA and sodium salts of alginic acid in stark contrast and again indicate that there are notable functional differences between both alginate binders.

We also carried out tests with the $LiFePO_4$ cathode for Li-ion batteries and found the results to be very similar (Supplementary Information, Chapter S6). PVDF outperforms TBA alginate binder in the LIB cell chemistry with 1M $LiPF_6$ electrolyte salt in the ethylene carbonate (EC)–dimethyl carbonate (DMC) mixture. Although the reasons for this require further investigation, we hypothesize that this behaviour could be due to instability of TBA alginate in the electrolyte used in LIB cell (1 M $LiPF_6$ in EC/DMC), resulting in the reduced mechanical integrity of the electrode and subsequent loss of electric contact between the current collector and active particles.

2.5. Analysis of Electrode-Electrolyte Interphase

To better understand the mechanisms for the apparently different behaviour between the three binders, we carried out electrochemical impedance (EIS) studies as well as SEM and XPS characterization of the cycled electrodes.

EIS results, shown in Figure 6, show the evolution of internal resistances. EIS data of uncycled cells, cells after formation (3 full charge-discharge cycles at a slow C-rate), and after 50 cycles at 1 C (175 mA/g) are shown. Two arcs are observed for all electrodes. The first corresponds to SEI resistance while the second to charge transfer processes [52,53], although the precise interpretation of these types of EIS results is still being disputed and might be more ambiguous [54,55]. As Gaberscek et al. have shown [54], in some cases, the high frequency arc can also correspond to electrode-current collector resistance rather than the SEI.
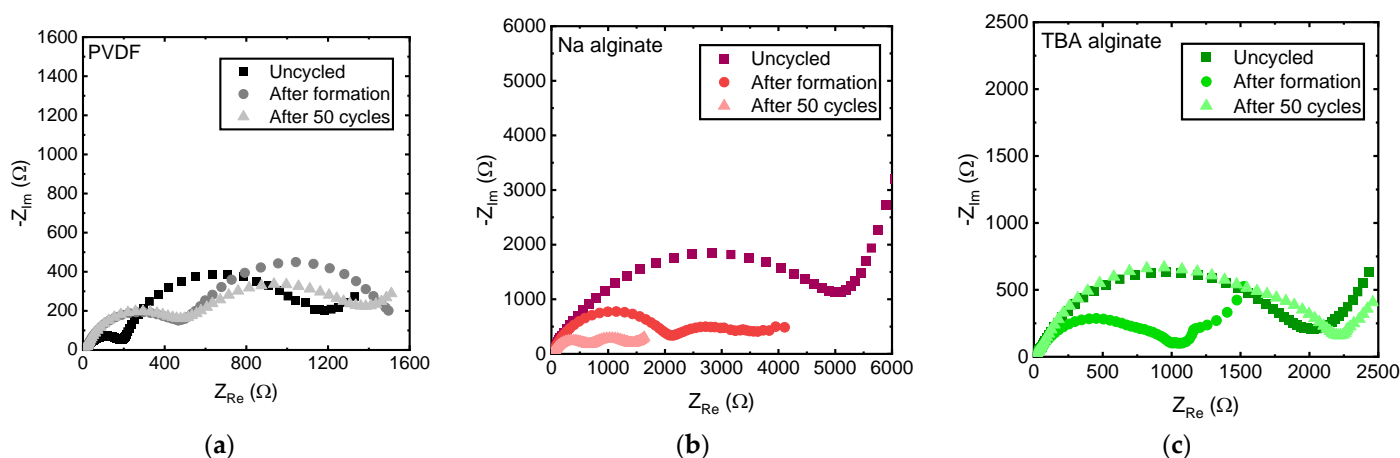

(a)

(b)

(c)

Figure 6. EIS spectra of $Na_{0.67}MnO_2$ electrodes prepared with (**a**) PVDF, (**b**) Na alginate and (**c**) TBA alginate binders, measured 3 h after assembly of the cell, after 3 formation cycles at a slow rate and after 50 cycles at 1 C (175 mA/g).

Looking at the EIS spectra individually (Figure 6a–c), we find that the internal resistances of PVDF-based electrode change relatively little, with SEI resistance increasing after formation, and charge transfer resistance slightly reducing after 50 cycles. The second semicircle of the EIS spectrum of the PVDF-based electrode flattens with cycling, pointing to the arising inhomogeneities, likely on the electrode's surface. Na alginate-based $Na_{0.67}MnO_2$ electrode undergoes significant changes, with both resistances notably shrinking during cycling. Both charge transfer and SEI resistances of TBA alginate-based electrode initially shrink similarly to the Na alginate-based electrode. However, after 50 cycles, an increase in the SEI resistance is observed.

When the EIS spectra are compared for similarly aged PVDF, Na alginate, and TBA alginate based $Na_{0.67}MnO_2$ electrodes, consistent with the lower gravimetric capacity and higher overvoltage values, Na alginate has the largest electrode resistance. However, it shrinks upon cycling, ultimately nearing that of the PVDF-based electrode. TBA alginate-based electrode displays significantly larger resistance.

SEM measurements of cycled electrodes, shown in Figure 7, indicate a considerably changed electrode morphology of PVDF-based electrodes, likely arising from a growth of a porous SEI. The surfaces of Na alginate and TBA alginate-based electrodes also display visible signs of SEI build-up (surface residue and smoother edges of grains can be observed). Cracks can be seen in Na alginate-based electrodes at some sites. However, this does not seem to be a widespread phenomenon. All in all, however, the all electrodes maintain their integrity, as the shape, size, or distribution of the active particles has not undergone any notable changes.
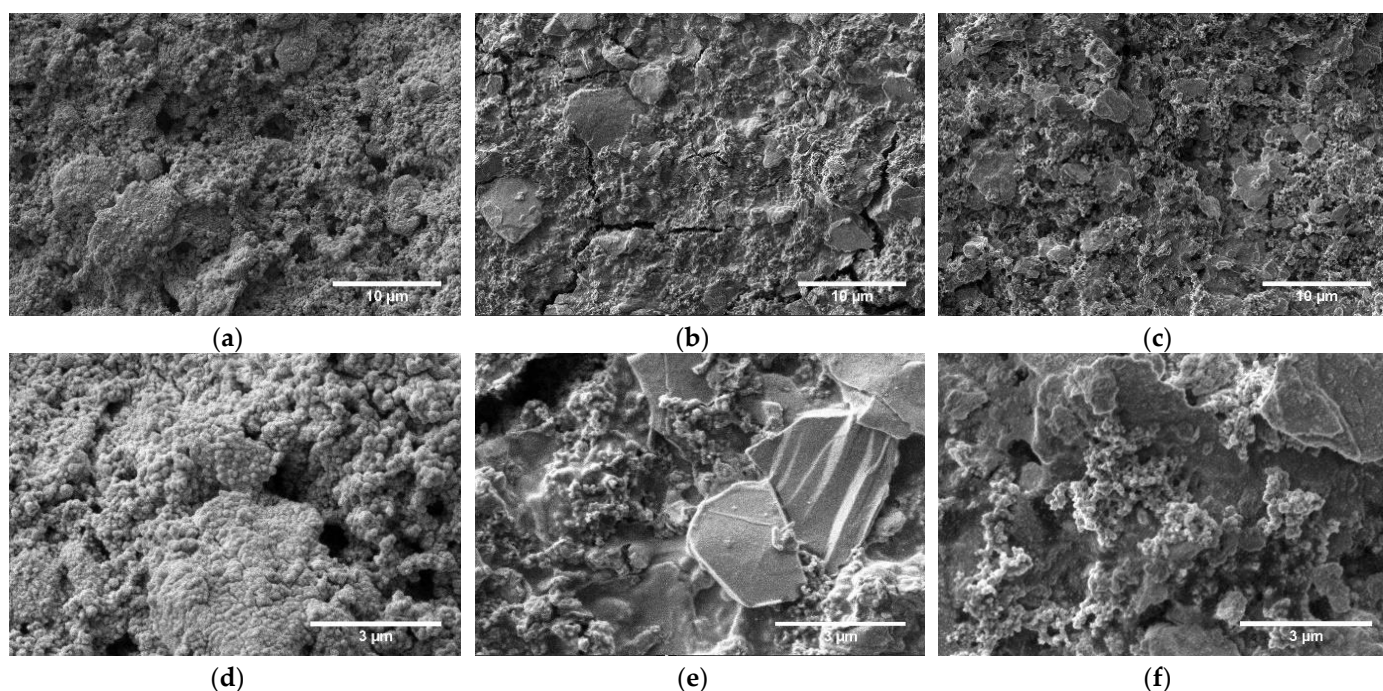
Figure 7. SEM of $Na_{0.67}MnO_2$ electrodes cycled at 1 C for 500 cycles, prepared with (**a**,**d**) PVDF; (**b**,**e**) Na alginate and (**c**,**f**) TBA alginate binders. The length of the scale bar is 10 μm for images in the top row and 3 μm for images in the bottom row.

Surfaces of cycled (500 cycles at 1 C) and uncycled electrodes were analysed with XPS (Figure 8). Typically, upon cycling, the solid–electrolyte interface (SEI) starts to grow, consuming some of the sodium and often increasing the internal resistance. The SEI is typically composed of NaF, Na_2O, Na_2CO_3, and other products of electrolyte and electrode decomposition.

NaF is a prominent part of the SEI. The XPS peak corresponding to Na-F bonding at 684.3 eV is observed for all the cycled electrodes. This is the result of the desirable decomposition of FEC electrolyte additive. The peak for C-F bonding (CF_2 in PVDF binder) at 688.2 eV is observed in fresh PVDF-based electrodes. Depth profiles of F indicate a considerable amount of F trapped in the SEI. The disappearance of C-F peak at 688.2 eV in the aged PVDF-based electrode again confirms the considerable thickness of the SEI, while the depth distribution of fluorine indicates a relatively higher fluorine content in TBA alginate and PVDF-based electrodes compared to Na alginate-based electrodes.

C1s peak can be deconvoluted into several peaks. Located at 284.8 eV is the peak associated with the C–C bonds of adventitious carbon and acetylene black. The peak at approximately 285.8 eV corresponds to hydrocarbon bonding (C-H), while peaks at 287.2, 289.2 and 290.7 eV are associated with C–O/C=O, Na_2CO_3 and $R–CO_3/CF_x$ ($x \geq 2$), respectively [49,56]. The shape and intensity of PVDF electrode changes significantly upon cycling, signalling a significant SEI growth, while that of Na alginate-based electrode remains virtually unchanged. The intensity of the TBA alginate electrode's peaks is lower for the aged electrode, but the shape remains unchanged and signals presence of mostly C–C and C–O/C=O bonds.

Mn signal measured for most electrodes is weaker in aged electrodes. This points to the formation of a SEI where Mn is not present. An exception to this is the PVDF-based electrodes, where the Mn signal in cycled electrode intensifies. The dissolution of Mn was previously observed In $Na_{0.67}MnO_2$ [57] and is likely more prevalent due to a more inhomogeneous SEI. This is in agreement with Zou et al. who have also reported formation of MnF_2 on the surface of a PVDF-based electrodes [21].
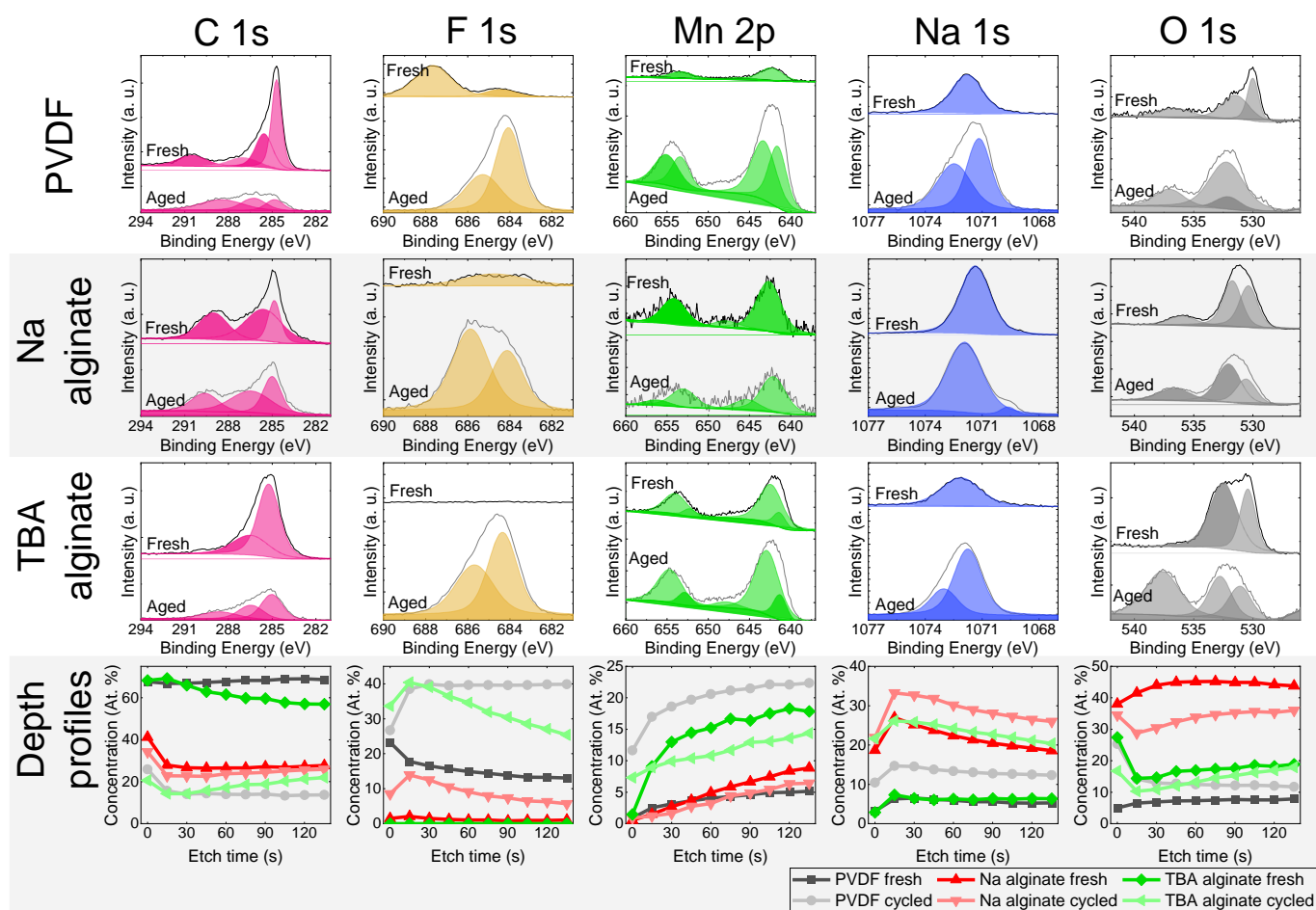
Figure 8. XPS results of $Na_{0.67}MnO_2$ electrodes for fresh and aged (cycled) electrodes that have undergone 500 charge-discharge cycles at 1 C (175 mA/g) rate—individual spectra and compositional analysis.

The signal of Na changes significantly when comparing fresh and cycled TBA alginate and PVDF alginate-based electrodes, again pointing towards a notable SEI growth, while the Na 1s spectrum of Na alginate-based electrode stays relatively similar for fresh and aged electrodes. Peaks of $ROCO_2Na$ (1070.3 eV), Na_2CO_3 (1071.5 eV), and NaF (1072.8 eV) are observed for Na. After the cycling, the peaks of Na shift to the right for PVDF and TBA alginate-based electrodes, pointing to an increasing intensity of $ROCO_2Na$ functional groups (1070.3 eV), although an appearance of NaF (1072.8 eV) is also observed. For Na alginate-based electrode, the shift is in the other direction, signifying a considerable prevalence of Na_2CO_3 (also evident from the C 1s spectrum). The Na concentration has increased considerably after cycling for PVDF and TBA alginate-based electrodes due to the SEI growth, while it remains similar for Na alginate-based electrode due to the binder containing significant amount of Na.

Oxygen signal contains several bands peaking at around 530 eV and 536 eV. The latter is the KLL line of Na. Oxygen spectra consist of peaks at 530.1, 531.8 eV, and 532.6 eV, corresponding to Na-O-Mn, Na_2CO_3, and RCH_2ONa respectively. While for the PVDF and Na alginate-based electrodes a large proportion comes from $Na_{0.67}MnO_2$ and Na_2CO_3, XPS data from TBA alginate-based electrode contain a considerably larger number of signals coming from RCH_2ONa.

To sum up, the results of the XPS point to the formation of a SEI that is Na- and F-rich and contains several organic compounds not seen in the fresh electrodes. Although TBA alginate does not contain fluorine, judging from the XPS results, it forms Na- and F-containing compounds on its surface that are similar to those observed on PVDF-based

electrode. In general, the difference between SEI formed on PVDF-based electrode and SEI formed on TBA alginate-based electrode is not large. On the other hand, Na alginate electrodes have less NaF in the SEI and generally undergo smaller compositional changes upon cycling.

3. Discussion

The set of results from structural, morphological, and interfacial characterisations combined with an array of electrochemical tests in different systems provide the first insight into the working mechanisms of TBA alginate binder.

Qualitatively, there are more functional similarities between TBA alginate and PVDF than between TBA and Na alginate binders. Electrodes based on PVDF and TBA alginate binders both follow a similar capacity decay pattern during the long-term charge-discharge cycling. Internal electrode resistances measured with EIS increase slightly during cycling, and electrodes based on both binders have a considerable amount of Na-F bonding in the SEI after cycling in 1 M $NaClO_4$ electrolyte with 5 wt.% FEC additive. XPS results indicate that the SEI grown on both TBA alginate- and PVDF-based electrodes contain considerable amounts of Na-F and RCH_2ONa compounds.

Perhaps the most notable difference between PVDF and TBA alginate-based electrodes is the porosity of the SEI, as evident in the SEM images. This is likely the reason why the observed SEI resistance measured by EIS is comparably largest for PVDF-based electrodes. Given the similar chemical composition of SEIs and good integrity of electrodes evidenced before and after long-term cycling experiments, it is likely that the improvement of the electrochemical properties of TBA alginate-based $Na_{0.67}MnO_2$ electrodes comes from an improved homogeneity of the SEI.

Interestingly, considerable functional differences exist between TBA and Na alginate electrodes. As evident from the XPS spectra (especially C, O and Na), Na alginate undergoes considerably less surface change upon ageing, pointing to an already-stable protective layer before cycling. The SEI layer seems to get richer in fluorine, with the SEI composition not limited only to NaF, and with it the resistance of the electrode reduces, as evidenced by EIS. Furthermore, when the Na alginate-based electrode is cycled in the electrolyte without FEC additive, the lack of NaF interfacial layer does not seem to affect the cycle life as much as that of the PVDF and TBA alginate-based electrodes. It can be hypothesized that Na alginate forms a more homogenous protective coating on the surface of the electrodes and thus prevents some of the undesirable decomposition reactions. The reason behind the radically different interfacial behaviours between TBA and Na alginate-based electrodes, however, remains a potentially interesting topic for future studies.

Naturally, challenges remain in optimising the process of mixing and coating the electrode slurries. In the present study, it took considerably longer to obtain a homogenous TBA alginate-based slurry than a comparable PVDF-based one. An interesting subject of practical future studies could be the performance of TBA alginate binder in conjunction with active materials that have an inherently better cycle life and do not suffer from Mn^{2+} dissolution and oxygen evolution as much as $Na_{0.67}MnO_2$ does. If work on $Na_{0.67}MnO_2$ is to be continued, several pathways could be considered for increasing cycle life of the cathode, as currently it falls below 50% of initial after 500 cycles. These pathways would most likely have to deal with mitigating the P2-P2′ and P2-OP4 phase transitions in the active material that have been shown to have a significant impact on the cycle life [21,29]. Approaches to stabilize the structure by modifying the crystal lattice [31] or via the doping or substitution of Mn or other elements have provided good results [46,58]. Further alterations of electrode formulations, i.e., electron-conducting additives [59], protective coatings [60], or the formation of various nanostructured materials, e.g., nanocomposites [61] or nanostructures with high specific surface area [62], could also be considered. Our study also opens up potential to further investigation and optimisation of the electrode slurries.

From a practical point of view, the use of TBA alginate binder instead of PVDF is appealing, as this research demonstrates the superior electrochemical performance of

the TBA alginate-based $Na_{0.67}MnO_2$ electrode when compared to PVDF binder-based electrodes, while measurements of electrode surface and SEI prior to and after cycling suggest these electrodes also possess good interfacial stability.

4. Materials and Methods

$Na_{0.67}MnO_2$ was prepared by solid-state synthesis. Stoichiometric amounts of Mn_2O_3 ($\geq$99%, Sigma-Aldrich, Darmstadt, Germany) and Na_2CO_3 ($\geq$99%, Sigma-Aldrich, Germany) were ball-milled for 2 h. The mixture was pressed into pellets and heated at 900 °C for 24 h in air. The samples were then cooled down to 500 °C, taken out of the furnace, and transferred to an Ar-filled glove box for further cooling and processing to avoid unnecessary contact with moisture, oxygen, and CO_2.

A procedure similar to that used by Babak et al. [34] and Pawar et al. [36] was followed. Thus, 120 mL 0.6 M HCl was mixed with 120 mL 96% ethanol. Na-alginate was added to the mixture and stirred for 12 h at 4 °C to obtain alginic acid. The mixture was filtered under vacuum and washed with alcohol and acetone. The solid product was dried in vacuum drying oven at 60 °C for 12 h.

1 g of fully dried alginic acid was dispersed in 150 mL water, then 1.5 M tetrabutylammonium hydroxide (TBA-OH) solution was added dropwise with continuous stirring at room temperature until the alginic acid was dissolved and the pH was adjusted to 8 ± 1. The mixture was dried in vacuum oven at 60 °C for 24 h until fully dry solid product was obtained.

The crystal structure of $Na_{0.67}MnO_2$ was characterized by X-ray diffraction (XRD) using Rigaku MiniFlex600 X-ray diffractometer with Cu Kα radiation at room temperature. The patterns were recorded in the 2θ range of 10–90°. Rietveld refinement was conducted with Bruker TOPAS software. An Agilent 8900 ICP-QQQ Inductively Coupled Plasma Mass Spectrometer (ICP-MS) equipped with a MicroMist nebulizer was used to determine Na and Mn ratio in $NaMnO_2$. Before measurements, $NaMnO_2$ was dissolved in nitric acid. Quantification of Na and Mn was done by 5-point calibration graph method in He mode. Scanning electron microscopy (SEM) images of $Na_{0.67}MnO_2$ powder and electrodes were taken by Thermo Scientific (Waltham, MA, USA) Helios 5 UX scanning electron microscope. Powders of the Na alginate, alginic acid and TBA alginate were analyzed with Fourier transformation infrared spectroscopy (FTIR) using Bruker Vertex 80v vacuum FTIR spectrometer.

X-ray photoelectron spectroscopy (XPS) was carried out for $Na_{0.67}MnO_2$ powder as well as battery electrodes before and after cycling (post-mortem) using ThermoFisher ESCALAB Xi+ instrument with monochromatic Al Kα X-ray source. The samples were transferred from the argon-filled glovebox to the XPS instrument in an inert gas transfer vessel. The instrument's binding energy scale was calibrated to give a binding energy at 932.6 eV for Cu $2p_{3/2}$ line of freshly etched metallic copper. A charge compensation system was used, with the surface of the sample irradiated with a flood of electrons to produce nearly neutral surface charge. The experimental data has been referenced to C 1s adventitious carbon. The spectra were recorded by using an X-ray beam size 650 $\times$ 10 microns, a pass energy of 20 eV and step size 0.1 eV.

The electrodes were prepared with wet slurry-coating method. The active material ($Na_{0.67}MnO_2$) was mixed with carbon black and binder (PVDF, Na alginate or TBA alginate) in a weight ratio of 75:15:10. Solvents N-methyl-2-pyrrolidone (NMP), water or N,N-dimethylformamide (DMF) were used respectively, the substances were mixed using mill mixer Retsch MM200. The obtained slurry was coated on an Al foil using a doctor blade and dried in a vacuum drying oven at 80 °C for 24 h.

The electrochemical performance was tested in Swagelok type cells assembled in Ar-filled glove box. Metallic sodium was used as counter electrode. Electrochemical cells were assembled, using glass fiber filter (Whatman GF/B) as separator and 1 M $NaClO_4$ solution in propylene carbonate (PC) with 5 wt.% fluoroethylene carbonate (FEC) as electrolyte. For selected measurements, described further in the text, the use of FEC

additive was avoided. Electrochemical measurements were carried out by using Biologic VMP3 potentiostat/galvanostat. Galvanostatic charge-discharge curves were obtained in constant current mode between 2 and 4 V. We assume 1 C charge/discharge current to correspond to 175 mA/g, based on the stoichiometry $Na_{0.67}MnO_2$.

Selected measurements with the PVDF and alginate binders were carried out in LIB cells following a procedure that is similar to the one described above. LIB cells consisted of metallic Li counter electrode, $LiFePO_4$ (LFP, battery grade, MTI Corp., Richmond, CA, USA) electrode ($LiFePO_4$:carbon black:binder ratio 75:15:10), Whatman GF/B separator and electrolyte, 1 M $LiPF_6$ in a mixture of ethylene carbonate (EC) and diethyl carbonate (DEC). The volume ratio of solvents was 1:1. Tests were carried out in the voltage range of 2.7–4.0 V.

For a post-mortem study, $Na_{0.67}MnO_2$ electrode was cycled at 1 C rate (175 mA/g) for 500 full charge-discharge cycles. To avoid contamination of the electrode surface, the experiments were carried out in an electrochemical cell without a separator. Cells were disassembled in an Ar-filled glovebox. Electrodes were rinsed in PC twice, 2 min each time, and dried before transferring to XPS in an inert-gas transfer tool to avoid air exposure. SEM images of the cycled electrodes were taken by using a Thermo Scientific Helios 5 UX scanning electron microscope.

5. Conclusions

$Na_{0.67}MnO_2$ electrode with TBA alginate binder for SIBs has been successfully prepared and characterised. The prepared $Na_{0.67}MnO_2$ electrode has a gravimetric capacity of up to 164 mAh/g (6% higher than electrode prepared with the current state-of-art binder—PVDF) and good rate capability and cyclability. To the best of our knowledge, this is the first study reporting TBA alginate as a binder in a battery application and is consequentially also the first alginate binder-based electrode prepared from a non-aqueous slurry. We conclude that TBA alginate-based electrodes, while somewhat tedious to prepare, display improved electrochemical performance when compared to PVDF-based electrodes. Therefore, TBA alginate is a good potential alternative to PVDF in battery applications where water-based processing of slurries is not feasible, such as the demonstrated case with $Na_{0.67}MnO_2$ cathode.

Institutional Review Board Statement: Not applicable.

Data Availability Statement: Data supporting reporting results available by request: gints.kucinskis@cfi.lu.lv.

Conflicts of Interest: The funders had no role in the design of the study; in the collection, analyses, or interpretation of data; in the writing of the manuscript, or in the decision to publish the results.

References

1. Vaalma, C.; Buchholz, D.; Weil, M.; Passerini, S. A cost and resource analysis of sodium-ion batteries. *Nat. Rev. Mater.* **2018**, *3*, 18013. [CrossRef]
2. Jin, T.; Li, H.; Zhu, K.; Wang, P.-F.; Liu, P.; Jiao, L. Polyanion-type cathode materials for sodium-ion batteries. *Chem. Soc. Rev.* **2020**, *49*, 2342–2377. [CrossRef]
3. Kucinskis, G.; Nesterova, I.; Sarakovskis, A.; Bikse, L.; Hodakovska, J.; Bajars, G. Electrochemical performance of $Na_2FeP_2O_7$/C cathode for sodium-ion batteries in electrolyte with fluoroethylene carbonate additive. *J. Alloys Compd.* **2022**, *895*, 162656. [CrossRef]
4. Lyu, Y.; Liu, Y.; Yu, Z.-E.; Su, N.; Liu, Y.; Li, W.; Li, Q.; Guo, B.; Liu, B. Recent advances in high energy-density cathode materials for sodium-ion batteries. *Sustain. Mater. Technol.* **2019**, *21*, e00098. [CrossRef]
5. Zhao, X.; Niketic, S.; Yim, C.-H.; Zhou, J.; Wang, J.; Abu-Lebdeh, Y. Revealing the Role of Poly(vinylidene fluoride) Binder in Si/Graphite Composite Anode for Li-Ion Batteries. *ACS Omega* **2018**, *3*, 11684–11690. [CrossRef]
6. Kubota, K.; Komaba, S. Review—Practical Issues and Future Perspective for Na-Ion Batteries. *J. Electrochem. Soc.* **2015**, *162*, A2538–A2550. [CrossRef]
7. Bresser, D.; Buchholz, D.; Moretti, A.; Varzi, A.; Passerini, S. Alternative binders for sustainable electrochemical energy storage—The transition to aqueous electrode processing and bio-derived polymers. *Energy Environ. Sci.* **2018**, *11*, 3096–3127. [CrossRef]
8. Kovalenko, I.; Zdyrko, B.; Magasinski, A.; Hertzberg, B.; Milicev, Z.; Burtovyy, R.; Luzinov, I.; Yushin, G. A Major Constituent of Brown Algae for Use in High-Capacity Li-Ion Batteries. *Science* **2011**, *334*, 75–79. [CrossRef] [PubMed]
9. Ge, M.; Rong, J.; Fang, X.; Zhou, C. Porous Doped Silicon Nanowires for Lithium Ion Battery Anode with Long Cycle Life. *Nano Lett.* **2012**, *12*, 2318–2323. [CrossRef] [PubMed]
10. Sethuraman, V.A.; Nguyen, A.; Chon, M.J.; Nadimpalli, S.P.V.; Wang, H.; Abraham, D.P.; Bower, A.F.; Shenoy, V.B.; Guduru, P.R. Stress Evolution in Composite Silicon Electrodes during Lithiation/Delithiation. *J. Electrochem. Soc.* **2013**, *160*, A739–A746. [CrossRef]
11. Xu, H.; Jiang, K.; Zhang, X.; Zhang, X.; Guo, S.; Zhou, H. Sodium Alginate Enabled Advanced Layered Manganese-Based Cathode for Sodium-Ion Batteries. *ACS Appl. Mater. Interfaces* **2019**, *11*, 26817–26823. [CrossRef] [PubMed]
12. Pan, H.; Lu, X.; Yu, X.; Hu, Y.-S.; Li, H.; Yang, X.-Q.; Chen, L. Sodium Storage and Transport Properties in Layered Na2Ti3O7 for Room-Temperature Sodium-Ion Batteries. *Adv. Energy Mater.* **2013**, *3*, 1186–1194. [CrossRef]
13. Darjazi, H.; Staffolani, A.; Sbrascini, L.; Bottoni, L.; Tossici, R.; Nobili, F. Sustainable Anodes for Lithium- and Sodium-Ion Batteries Based on Coffee Ground-Derived Hard Carbon and Green Binders. *Energies* **2020**, *13*, 6216. [CrossRef]
14. Wang, P.-F.; You, Y.; Yin, Y.-X.; Guo, Y.-G. Layered Oxide Cathodes for Sodium-Ion Batteries: Phase Transition, Air Stability, and Performance. *Adv. Energy Mater.* **2018**, *8*, 1701912. [CrossRef]
15. Kumakura, S.; Tahara, Y.; Kubota, K.; Chihara, K.; Komaba, S. Sodium and Manganese Stoichiometry of P2-Type $Na_{2/3}MnO_2$. *Angew. Chemie Int. Ed.* **2016**, *55*, 12760–12763. [CrossRef]
16. Paulsen, J.M.; Dahn, J.R. Studies of the layered manganese bronzes, $Na_{2/3}[Mn_{1-x}M_x]O_2$ with M=Co, Ni, Li, and $Li_{2/3}[Mn_{1-x}M_x]O_2$ prepared by ion-exchange. *Solid State Ion.* **1999**, *126*, 3–24. [CrossRef]
17. Luo, C.; Langrock, A.; Fan, X.; Liang, Y.; Wang, C. P2-type transition metal oxides for high performance Na-ion battery cathodes. *J. Mater. Chem. A* **2017**, *5*, 18214–18220. [CrossRef]
18. Lyu, Y.-Q.; Yu, J.; Wu, J.; Effat, M.B.; Ciucci, F. Stabilizing Na-metal batteries with a manganese oxide cathode using a solid-state composite electrolyte. *J. Power Sources* **2019**, *416*, 21–28. [CrossRef]
19. Zhou, Z.; Li, J.; Luo, Z.; He, Z.; Zheng, J.; Li, Y.; Mao, J.; Dai, K.; Yan, C.; Sun, Z. $Na_{2/3}MnO_2$ nanoplates with exposed active planes as superior electrochemical performance sodium-ion batteries. *Ionics* **2021**, *27*, 5187–5196. [CrossRef]
20. Jung, E.; Park, Y.; Park, K.; Kwon, M.-S.; Park, M.; Sinha, A.K.; Lee, B.-H.; Kim, J.; Lee, H.S.; Chae, S.I.; et al. Synthesis of nanostructured P2-$Na_{2/3}MnO_2$ for high performance sodium-ion batteries. *Chem. Commun.* **2019**, *55*, 4757–4760. [CrossRef]
21. Zuo, W.; Qiu, J.; Liu, X.; Zheng, B.; Zhao, Y.; Li, J.; He, H.; Zhou, K.; Xiao, Z.; Li, Q.; et al. Highly-stable P2–$Na_{0.67}MnO_2$ electrode enabled by lattice tailoring and surface engineering. *Energy Storage Mater.* **2020**, *26*, 503–512. [CrossRef]

22. Konarov, A.; Kim, H.J.; Voronina, N.; Bakenov, Z.; Myung, S.-T. P2-Na$_{2/3}$MnO$_2$ by Co Incorporation: As a Cathode Material of High Capacity and Long Cycle Life for Sodium-Ion Batteries. *ACS Appl. Mater. Interfaces* **2019**, *11*, 28928–28933. [CrossRef] [PubMed]

23. Hemalatha, K.; Jayakumar, M.; Bera, P.; Prakash, A.S. Improved electrochemical performance of Na$_{0.67}$MnO$_2$ through Ni and Mg substitution. *J. Mater. Chem. A* **2015**, *3*, 20908–20912. [CrossRef]

24. Zuo, W.; Qiu, J.; Liu, X.; Ren, F.; Liu, H.; He, H.; Luo, C.; Li, J.; Ortiz, G.F.; Duan, H.; et al. The stability of P2-layered sodium transition metal oxides in ambient atmospheres. *Nat. Commun.* **2020**, *11*, 3544. [CrossRef] [PubMed]

25. Xiao, J.; Li, X.; Tang, K.; Wang, D.; Long, M.; Gao, H.; Chen, W.; Liu, C.; Liu, H.; Wang, G. Recent progress of emerging cathode materials for sodium ion batteries. *Mater. Chem. Front.* **2021**, *5*, 3735–3764. [CrossRef]

26. Abraham, K.M. How Comparable Are Sodium-Ion Batteries to Lithium-Ion Counterparts? *ACS Energy Lett.* **2020**, *5*, 3544–3547. [CrossRef]

27. Yabuuchi, N.; Kajiyama, M.; Iwatate, J.; Nishikawa, H.; Hitomi, S.; Okuyama, R.; Usui, R.; Yamada, Y.; Komaba, S. P2-type Na$_x$[Fe$_{1/2}$Mn$_{1/2}$]O$_2$ made from earth-abundant elements for rechargeable Na batteries. *Nat. Mater.* **2012**, *11*, 512–517. [CrossRef] [PubMed]

28. Billaud, J.; Singh, G.; Armstrong, A.R.; Gonzalo, E.; Roddatis, V.; Armand, M.; Rojo, T.; Bruce, P.G. Na$_{0.67}$Mn$_{1-x}$Mg$_x$O$_2$ ($0 \le x \le 0.2$): A high capacity cathode for sodium-ion batteries. *Energy Environ. Sci.* **2014**, *7*, 1387–1391. [CrossRef]

29. Liu, X.; Zuo, W.; Zheng, B.; Xiang, Y.; Zhou, K.; Xiao, Z.; Shan, P.; Shi, J.; Li, Q.; Zhong, G.; et al. P2-Na$_{0.67}$Al$_x$Mn$_{1-x}$O$_2$: Cost-Effective, Stable and High-Rate Sodium Electrodes by Suppressing Phase Transitions and Enhancing Sodium Cation Mobility. *Angew. Chemie Int. Ed.* **2019**, *58*, 18086–18095. [CrossRef]

30. Clément, R.J.; Bruce, P.G.; Grey, C.P. Review—Manganese-Based P2-Type Transition Metal Oxides as Sodium-Ion Battery Cathode Materials. *J. Electrochem. Soc.* **2015**, *162*, A2589–A2604. [CrossRef]

31. Zuo, W.; Liu, X.; Qiu, J.; Zhang, D.; Xiao, Z.; Xie, J.; Ren, F.; Wang, J.; Li, Y.; Ortiz, G.F.; et al. Engineering Na$^+$-layer spacings to stabilize Mn-based layered cathodes for sodium-ion batteries. *Nat. Commun.* **2021**, *12*, 4903. [CrossRef] [PubMed]

32. Monyoncho, E.; Bissessur, R. Unique properties of α-NaFeO$_2$: De-intercalation of sodium via hydrolysis and the intercalation of guest molecules into the extract solution. *Mater. Res. Bull.* **2013**, *48*, 2678–2686. [CrossRef]

33. Duffort, V.; Talaie, E.; Black, R.; Nazar, L.F. Uptake of CO$_2$ in Layered P2-Na$_{0.67}$Mn$_{0.5}$Fe$_{0.5}$O$_2$: Insertion of Carbonate Anions. *Chem. Mater.* **2015**, *27*, 2515–2524. [CrossRef]

34. Babak, V.G.; Skotnikova, E.A.; Lukina, I.G.; Pelletier, S.; Hubert, P.; Dellacherie, E. Hydrophobically Associating Alginate Derivatives: Surface Tension Properties of Their Mixed Aqueous Solutions with Oppositely Charged Surfactants. *J. Colloid Interface Sci.* **2000**, *225*, 505–510. [CrossRef]

35. Leone, G.; Torricelli, P.; Chiumiento, A.; Facchini, A.; Barbucci, R. Amidic alginate hydrogel for nucleus pulposus replacement. *J. Biomed. Mater. Res. Part A* **2008**, *84A*, 391–401. [CrossRef]

36. Pawar, S.N.; Edgar, K.J. Chemical Modification of Alginates in Organic Solvent Systems. *Biomacromolecules* **2011**, *12*, 4095–4103. [CrossRef]

37. Ramana, C.V.; Massot, M.; Julien, C.M. XPS and Raman spectroscopic characterization of LiMn$_2$O$_4$ spinels. *Surf. Interface Anal.* **2005**, *37*, 412–416. [CrossRef]

38. Murray, J.W.; Dillard, J.G.; Giovanoli, R.; Moers, H.; Stumm, W. Oxidation of Mn(II): Initial mineralogy, oxidation state and ageing. *Geochim. Cosmochim. Acta* **1985**, *49*, 463–470. [CrossRef]

39. Junta, J.L.; Hochella, M.F. Manganese (II) oxidation at mineral surfaces: A microscopic and spectroscopic study. *Geochim. Cosmochim. Acta* **1994**, *58*, 4985–4999. [CrossRef]

40. Lee, G.; Song, K.; Bae, J. Permanganate oxidation of arsenic(III): Reaction stoichiometry and the characterization of solid product. *Geochim. Cosmochim. Acta* **2011**, *75*, 4713–4727. [CrossRef]

41. Namgung, S.; Chon, C.-M.; Lee, G. Formation of diverse Mn oxides: A review of bio/geochemical processes of Mn oxidation. *Geosci. J.* **2018**, *22*, 373–381. [CrossRef]

42. Schleeh, T.; Madau, M.; Roessner, D. Synthesis enhancements for generating highly soluble tetrabutylammonium alginates in organic solvents. *Carbohydr. Polym.* **2014**, *114*, 493–499. [CrossRef]

43. Han, M.H.; Sharma, N.; Gonzalo, E.; Pramudita, J.C.; Brand, H.E.A.; López del Amo, J.M.; Rojo, T. Moisture exposed layered oxide electrodes as Na-ion battery cathodes. *J. Mater. Chem. A* **2016**, *4*, 18963–18975. [CrossRef]

44. Shan, X.; Guo, F.; Charles, D.S.; Lebens-Higgins, Z.; Abdel Razek, S.; Wu, J.; Xu, W.; Yang, W.; Page, K.L.; Neuefeind, J.C.; et al. Structural water and disordered structure promote aqueous sodium-ion energy storage in sodium-birnessite. *Nat. Commun.* **2019**, *10*, 4975. [CrossRef] [PubMed]

45. Hemalatha, K.; Jayakumar, M.; Prakash, A.S. Influence of the manganese and cobalt content on the electrochemical performance of P2-Na$_{0.67}$Mn$_x$Co$_{1-x}$O$_2$ cathodes for sodium-ion batteries. *Dalt. Trans.* **2018**, *47*, 1223–1232. [CrossRef] [PubMed]

46. Peng, B.; Sun, Z.; Jiao, S.; Wang, G.; Zhang, G. Electrochemical Performance Optimization of Layered P2-Type Na$_{0.67}$MnO$_2$ through Simultaneous Mn-Site Doping and Nanostructure Engineering. *Batter. Supercaps* **2020**, *3*, 147–154. [CrossRef]

47. Liu, L.; An, M.; Yang, P.; Zhang, J. Superior cycle performance and high reversible capacity of SnO$_2$/graphene composite as an anode material for lithium-ion batteries. *Sci. Rep.* **2015**, *5*, 9055. [CrossRef]

48.　Pandit, B.; Rondiya, S.R.; Dzade, N.Y.; Shaikh, S.F.; Kumar, N.; Goda, E.S.; Al-Kahtani, A.A.; Mane, R.S.; Mathur, S.; Salunkhe, R.R. High Stability and Long Cycle Life of Rechargeable Sodium-Ion Battery Using Manganese Oxide Cathode: A Combined Density Functional Theory (DFT) and Experimental Study. *ACS Appl. Mater. Interfaces* **2021**, *13*, 11433–11441. [CrossRef]

49.　Vogt, L.O.; El Kazzi, M.; Jämstorp Berg, E.; Pérez Villar, S.; Novák, P.; Villevieille, C. Understanding the Interaction of the Carbonates and Binder in Na-Ion Batteries: A Combined Bulk and Surface Study. *Chem. Mater.* **2015**, *27*, 1210–1216. [CrossRef]

50.　Luque, G.L.; Li, Y.; Zeng, X.; Luo, X.; Leiva, E.P.M.; Chen, Z.; Amine, K. Impact of alginate and fluoroethylene carbonate on the electrochemical performance of SiO–SnCoC anode for lithium-ion batteries. *J. Solid State Electrochem.* **2019**, *23*, 397–405. [CrossRef]

51.　Ling, L.; Bai, Y.; Wang, Z.; Ni, Q.; Chen, G.; Zhou, Z.; Wu, C. Remarkable Effect of Sodium Alginate Aqueous Binder on Anatase TiO2 as High-Performance Anode in Sodium Ion Batteries. *ACS Appl. Mater. Interfaces* **2018**, *10*, 5560–5568. [CrossRef]

52.　Barsoukov, E.; Macdonald, J.R. *Impedance Spectroscopy: Theory, Experiment and Applications*, 2nd ed.; Barsoukov, E., Macdonald, J.R., Eds.; Wiley: Hoboken, NJ, USA, 2005; ISBN 9780471647492.

53.　Dees, D.; Gunen, E.; Abraham, D.; Jansen, A.; Prakash, J. Alternating Current Impedance Electrochemical Modeling of Lithium-Ion Positive Electrodes. *J. Electrochem. Soc.* **2005**, *152*, A1409. [CrossRef]

54.　Atebamba, J.-M.; Moskon, J.; Pejovnik, S.; Gaberscek, M. On the Interpretation of Measured Impedance Spectra of Insertion Cathodes for Lithium-Ion Batteries. *J. Electrochem. Soc.* **2010**, *157*, A1218. [CrossRef]

55.　Gaberšček, M. Understanding Li-based battery materials via electrochemical impedance spectroscopy. *Nat. Commun.* **2021**, *12*, 6513. [CrossRef]

56.　Shkrob, I.A.; Zhu, Y.; Marin, T.W.; Abraham, D. Reduction of Carbonate Electrolytes and the Formation of Solid-Electrolyte Interface (SEI) in Lithium-Ion Batteries. 1. Spectroscopic Observations of Radical Intermediates Generated in One-Electron Reduction of Carbonates. *J. Phys. Chem. C* **2013**, *117*, 19255–19269. [CrossRef]

57.　Caballero, A.; Hernán, L.; Morales, J.; Sánchez, L.; Santos Peña, J.; Aranda, M.A.G. Synthesis and characterization of high-temperature hexagonal P2-$Na_{0.6}MnO_2$ and its electrochemical behaviour as cathode in sodium cells. *J. Mater. Chem.* **2002**, *12*, 1142–1147. [CrossRef]

58.　Hou, H.; Gan, B.; Gong, Y.; Chen, N.; Sun, C. P2-Type $Na_{0.67}Ni_{0.23}Mg_{0.1}Mn_{0.67}O_2$ as a High-Performance Cathode for a Sodium-Ion Battery. *Inorg. Chem.* **2016**, *55*, 9033–9037. [CrossRef]

59.　Zhang, Q.; Yu, Z.; Du, P.; Su, C. Carbon Nanomaterials Used as Conductive Additives in Lithium Ion Batteries. *Recent Pat. Nanotechnol.* **2010**, *4*, 100–110. [CrossRef] [PubMed]

60.　Somo, T.R.; Mabokela, T.E.; Teffu, D.M.; Sekgobela, T.K.; Ramogayana, B.; Hato, M.J.; Modibane, K.D. A Comparative Review of Metal Oxide Surface Coatings on Three Families of Cathode Materials for Lithium Ion Batteries. *Coatings* **2021**, *11*, 744. [CrossRef]

61.　Kucinskis, G.; Bajars, G.; Bikova, K.; Kaprans, K.; Kleperis, J. Microstructural Influence on Electrochemical Properties of LiFePO4/C/Reduced Graphene Oxide Composite Cathode. *Russ. J. Electrochem.* **2019**, *55*, 517–523. [CrossRef]

62.　Liu, J.; Tang, K.; Song, K.; van Aken, P.A.; Yu, Y.; Maier, J. Electrospun $Na_3V_2(PO_4)_3$/C nanofibers as stable cathode materials for sodium-ion batteries. *Nanoscale* **2014**, *6*, 5081. [CrossRef] [PubMed]